Computers and Fluids 000 (2018) 1–13

Contents lists available at ScienceDirect

Computers and Fluids

journal homepage: www.elsevier.com/locate/compfluid

Benchmark solutions

A semi-Lagrangian splitting method for the numerical simulation of sediment transport with free surface flows

Sébastien Boyaval[a], Alexandre Caboussat[b,*], Arwa Mrad[c], Marco Picasso[c], Gilles Steiner[c,d]

[a] Laboratoire d'hydraulique Saint-Venant, Université Paris-Est (Ecole des Ponts), Chatou Cedex 78401, France
[b] Geneva School of Business Administration, University of Applied Sciences Western Switzerland (HES-SO), Carouge 1227, Switzerland
[c] Mathematics Institute, Ecole polytechnique fédérale de Lausanne, Lausanne 1015, Switzerland
[d] Ycoor Systems SA, Sierre 3960, Switzerland

ARTICLE INFO

Article history:
Received 15 January 2018
Revised 27 March 2018
Accepted 2 April 2018
Available online xxx

MSC:
65M60
65M08
65M55
76D05
76T10

Keywords:
Particle flow
Sediment transport
Mixture model
Free surface flow
Operator splitting

ABSTRACT

We present a numerical model for the simulation of 3D poly-dispersed sediment transport in a Newtonian flow with free surfaces. The physical model is based on a mixture model for multiphase flows. The Navier–Stokes equations are coupled with the transport and deposition of the particle concentrations, and a volume-of-fluid approach to track the free surface between water and air. The numerical algorithm relies on operator-splitting to decouple advection and diffusion phenomena. Two grids are used, based on unstructured finite elements for diffusion and an appropriate combination of the characteristics method with Godunov's method for advection on a structured grid. The numerical model is validated through numerical experiments. Simulation results are compared with experimental results in various situations for mono-disperse and bi-disperse sediments, and the calibration of the model is performed using, in particular, erosion experiments.

1. Introduction

The modeling of sediment transport in rivers, lakes or shores is particularly relevant in hydraulic engineering to determine the amount and location of granular matters in the liquid. Sediments have indeed an influence on structural damages, operations efficiency and management, but also influence the efficiency of energy production in dam retention lakes. Moreover, the accumulation of river sediments in certain areas of the rivers modifies the natural environment, which might have important consequences for hydraulic energy production [1] or environmental regulations.

The modeling of sediment transport in a flow classically relies on a multiphase model. Two-phase flow models [2–4] use a second liquid field for the dilute sediment phase, with a different momentum equation in addition to that of the first liquid field, and possibly with a different rheology. The other alternatives are to macroscopically model the sediment concentration by an additional concentration field [5,6], which is well-validated at low concentration levels, or via the modeling of individual sediment particles at the microscopic level [7,8].

We focus here on sediments in suspension or accumulated in a Newtonian fluid (typically water). We investigate a macroscopic model for the sediment transport based on a sediment concentration with a single momentum balance for the mixture. The dilute concentration of sediments oscillates between zero and a maximal concentration corresponding to consolidated sediments.

The model proposed here couples the Navier–Stokes equations, with a volume-of-fluid approach for the tracking of the free surfaces between water and air, plus a nonlinear advection equation for the sediments' migration from low to high concentration areas. Since both dilute and undilute sediment concentrations in the liquid need to be described, a model able to describe not only the two phases but also the migration of the sediments from high to low concentration areas, and the resulting density variations, is chosen. This requires a *miscible model*, by opposition with, e.g., immiscible multiphase flow model [9]. As opposed to [9], here the advection equation for the tracers is *nonlinear* and concentrations vary along the Lagrangian trajectories.

* Corresponding author.
E-mail address: alexandre.caboussat@hesge.ch (A. Caboussat).

https://doi.org/10.1016/j.compfluid.2018.04.002

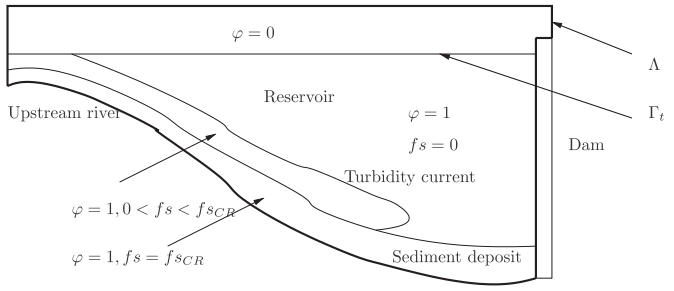

Fig. 1. Dam retention lake including sediment transport and deposition. 2D sketch of the geometrical domain.The cavity Λ is highlighted in bold. At each time $t \in (0, T)$, the liquid domain Ω_t is separated from the ambient air by the water-air interface Γ_t. The water domain is described by its characteristic function φ, while the sediment concentration fs is bounded in the liquid by its maximal value fs_{CR}.

A mathematical model for the simulation of Newtonian fluids with free surfaces, without sediment transport, has been presented and validated in [10–13], and has been applied to hydraulic engineering situations in [14]. It is extended here to include sediment transport. The addition of sediments has a direct effect on the density and viscosity of the flow. Reciprocally, the velocity of the flow is used to transport the sediment concentration, in addition to deposition effects due to the gravity.

An operator splitting approach allows to decouple the diffusion operator, the advection operator (by the mixture velocity) and the nonlinear transport operator for sediment deposition. A two-grids method couples a finite element discretization for the solution of a Stokes problem, with a finer structured grid of small cells for the discretization of advection operators and sediment deposition. While finite elements techniques are used for the approximation of the Stokes problem, a characteristics method and a Godunov method are used for the approximation of the linear and nonlinear transport problems respectively. Several numerical experiments validate the mathematical model presented in this work, starting with benchmark situations in simple geometries to real experiments for erosion problems, in which computational results are benchmarked against experimental results. Mono- and bi-disperse sediments are considered, and sensitivity analyses are performed.

The novelty of the proposed approach lies in the choice of a dedicated numerical method proposed to solve this multiphysics model, which couples sediment transport and free surfaces. The advocated splitting algorithm efficiently decouples the various physical phenomena and addresses each of them with dedicated techniques, involving finite elements, finite volumes and characteristics methods. Furthermore, there is no explicit tracking of the interfaces. The free surface between water and air is modeled by an Eulerian (volume-of-fluid) approach, while a diffuse interface modeling is used for the interface between water and the sediments.

This article is structured as follows. In Section 2, we describe the mathematical model for coupling the evolution of a Newtonian fluid with free surfaces with sediment transport. Sections 3 and 4 detail respectively the time and space discretizations. The results of numerical experiments for various test cases are presented in Section 5.

2. Mathematical model

Let us consider Λ a bounded domain in $\mathbb{R}^3$ with a sufficiently smooth boundary. Typically, we can consider a water reservoir or a dam retention lake, a sketch of which is illustrated in Fig. 1 in two space dimensions.

Let $T > 0$ be the final time of simulation. For any given time $t \in (0, T)$, let $\Omega_t \subset \Lambda$ be the domain occupied by the fluid (mixture including sediments), so that the remaining part of the domain Λ is occupied by the ambient air. Let Γ_t be the free surface between the liquid and the ambient air; it is defined by $\Gamma_t := \partial\Omega_t \backslash \partial\Lambda$ (namely the boundary of the liquid domain that is not in contact with the boundary of the whole cavity).

The mathematical model reads as follows. First let us describe the set of unknowns. Let Q_T denote the space-time domain containing the liquid, that is $Q_T = \{(\mathbf{x}, t) : \mathbf{x} \in \Omega_t, 0 < t < T\}$. The liquid domain is described by its characteristic function φ: $\Lambda \times (0, T) \to \{0, 1\}$, which implies that $Q_T = \{(\mathbf{x}, t) \in \Lambda \times (0, T) : \varphi(\mathbf{x}, t) = 1\}$. Assuming that the liquid domain Q_T is known and sufficiently regular, in the liquid region, the velocity field $\mathbf{v} : Q_T \to \mathbb{R}^3$ and the pressure field $p : Q_T \to \mathbb{R}$ are assumed to satisfy time-dependent, incompressible Navier–Stokes equations, with variable density and viscosity coefficients, and an additional Darcy-like reaction term modeling the porous solid matrix [15,16]. Finally, for the various classes of sediments, the sediment concentrations are defined in the liquid domain as $fs_i : Q_T \to [0, fs_{CR}]$, where fs_{CR} is the maximal sediment concentration. The set of corresponding equations read as follows. The evolution of the mixture (water and sediments) domain $\Omega_t \subset \Lambda$ is modeled by means of a volume-of-fluid method. Let $\varphi : \Lambda \times (0, T) \to \mathbb{R}$ be the characteristic function of the liquid domain Q_T. The function φ equals one at the point $(\mathbf{x}, t)$ if the liquid is present, zero if it is not. In order to describe the kinematics of the free surface, φ must satisfy (in a weak sense):

$$\frac{\partial \varphi}{\partial t} + \mathbf{v} \cdot \nabla \varphi = 0 \qquad \text{in } \Lambda \times (0, T), \tag{2.1}$$

where $\mathbf{v}$ outside Q_T is a regular extension of $\mathbf{v}$ inside Q_T (see, *e.g.*, [17]). More precisely, $\mathbf{v}(\mathbf{X}(t), t) = \mathbf{v}(\mathbf{X}(0), 0)$, where $\mathbf{X}(t)$ is the trajectory of a fluid particle which is at position $\mathbf{X}(0)$ at time $t = 0$, thus $\mathbf{X}'(t) = \mathbf{v}(\mathbf{X}(t), t)$.

The characteristic function of the liquid domain φ is given at initial time, which is equivalent to defining the initial liquid region $\Omega_0 = \{\mathbf{x} \in \Lambda : \varphi(\mathbf{x}, 0) = 1\}$. The initial velocity field $\mathbf{v}$ is prescribed in Ω_0 (see below), and boundary conditions are given on the inlet part of $\partial\Omega$.

Together, we consider a poly-dispersed model for the miscible sediment in the liquid. Assuming M populations of sediments (differing by size and/or density and/or shape), the presence rate of a sediment population is denoted by the solid fractions $fs_i : Q_T \to [0, 1]$ for $i = 1, \ldots, M$. This presence rate is a percentage of solid sediment in a given volume. The total amount of sediment

$$fs = \sum_{i=1}^{M} fs_i$$

is actually limited by a critical maximum value $fs_{CR} < 1$ that essentially depends on the shape of the sediment particles. In practise, if we consider a mono-disperse model with solid spherical particles and without consolidation, this value is approximately equal to 0.63.

We assume the liquid mixture velocity and pressure $\mathbf{v} : Q_T \to \mathbb{R}^3$ and $p : Q_T \to \mathbb{R}$ satisfy, in Q_T:

$$\rho(fs)\frac{\partial \mathbf{v}}{\partial t} + \rho(fs)(\mathbf{v} \cdot \nabla)\mathbf{v} - 2\nabla \cdot (\mu(fs)\mathbf{D}(\mathbf{v})) + \alpha(fs)\mathbf{v} + \nabla p = \rho(fs)\mathbf{g}, \tag{2.2}$$

$$\nabla \cdot \mathbf{v} = 0. \tag{2.3}$$

Here $\mathbf{D}(\mathbf{v}) = 1/2(\nabla \mathbf{v} + \nabla \mathbf{v}^T)$ is the symmetric deformation tensor, $\mathbf{g}$ denotes the gravity field, and $\rho(fs)$ (resp. $\mu(fs)$) is the density (resp. viscosity) of the fluid-sediment mixture. The coefficient $\alpha(fs)$ is a Darcy-like penalization term. All physical coefficients depend on the sediment concentrations fs_i, $i = 1, \ldots, M$. More precisely,

Please cite this article as: S. Boyaval et al., A semi-Lagrangian splitting method for the numerical simulation of sediment transport with free surface flows, Computers and Fluids (2018), https://doi.org/10.1016/j.compfluid.2018.04.002

the density $\rho = \rho(fs_1, \ldots, fs_M)$ is given by a linear weighted combination of the individual densities ρ_i:

$$\rho = \rho_l(1 - fs) + \sum_{i=1}^{M} \rho_i fs_i, \tag{2.4}$$

where ρ_l (resp. ρ_i) is the fluid density (resp. the density of sediment i). For the sake of notation, $\rho(fs_1, \ldots, fs_M)$ is still denoted by $\rho(fs)$. The viscosity $\mu = \mu(fs)$, represents the apparent viscosity of the fluid with the suspended particles; it is modeled with the so-called Ishii and Zuber law for particle flows [18]:

$$\mu(fs) = \begin{cases} \mu_l \left(1 - \dfrac{fs}{fs_{CR}}\right)^{-2.5\ fs_{CR}}, & \text{if } fs < fs_{CO}, \\ \mu_l \left(1 - \dfrac{fs_{CO}}{fs_{CR}}\right)^{-2.5\ fs_{CR}}, & \text{otherwise.} \end{cases} \tag{2.5}$$

where fs_{CO} is a cohesion threshold parameter to be calibrated. The choice of (2.5) is validated in the literature for small values of the concentration fs. Moreover, the velocity in the Navier–Stokes equations is penalized with a Brinkman term using Carman–Kozeny empirical law, which represents the coupling with Darcy flow in porous media. The reaction coefficient $\alpha = \alpha(fs)$ in (2.2) is given by:

$$\alpha(fs) = K \frac{\mu_l\, fs^2}{d_*^2\ (fs_{CR} - fs)^3 + \varepsilon}, \tag{2.6}$$

where K and ε are constants to be calibrated (in the numerical experiments, we consider $K = 1$ and vary ε), and d_* is the local mean particle diameter computed as

$$d_* = \sum_{i=1}^{M} \frac{fs_i}{fs} d_i. \tag{2.7}$$

Note that, practically, the parameter ε $(0 < \varepsilon \ll 1)$ avoids a division by zero when $fs = fs_{CR}$ in (2.6).

The Navier-Stokes equations (2.2)–(2.3) are completed with initial and boundary conditions. The initial conditions for the velocity are

$$\mathbf{v}(0) = \mathbf{v}_0, \qquad \text{in} \quad \Omega_0,$$

while slip or no-slip boundary conditions are imposed on the boundary of the liquid domain $\partial\Omega_t$ that is in contact with the boundary of the cavity $\partial\Lambda$. Surface tension effects on the liquid-gas interface are not taken into account, and the ambient air is supposed to have no influence on the liquid, and is treated as vacuum. The boundary conditions on the liquid-gas interface are thus given by the no-force boundary condition:

$$-p\mathbf{n}_\Gamma + 2\mu(fs)\mathbf{D}(\mathbf{v})\mathbf{n}_\Gamma = 0, \qquad \text{on} \quad \Gamma_t = \partial\Omega_t \backslash \partial\Lambda. \tag{2.8}$$

with $\mathbf{n}_\Gamma$ the external normal vector to Γ.

The sedimentation transport model for each population of particles reads as follows: for $i = 1, \ldots, M$, the solid fraction $fs_i : Q_T \to \mathbb{R}$ satisfy:

$$\frac{\partial fs_i}{\partial t} + \mathbf{v} \cdot \nabla fs_i + \nabla \cdot \mathbf{F}(fs_i) = 0, \quad i = 1 \ldots, M, \quad \text{in} \quad Q_T, \tag{2.9}$$

where $\mathbf{F}(fs_i)$ is a deposition flux. Various multiphase models for this deposition flux exist in the literature. Here, this flux is given by:

$$\mathbf{F}(fs_i) = \kappa fs_i \left(1 - \frac{fs_i}{fs_{CR}}\right) v_{stokes,i} \frac{\mathbf{g}}{||\mathbf{g}||_2}, \tag{2.10}$$

where κ is a constant independent from fs_i, $v_{stokes,\,i}$ is the maximal sediment velocity given by the Stokes' law:

$$v_{stokes,i} = \frac{d_i^2 ||\mathbf{g}||_2 (\rho_i - \rho_l)}{18\mu_l}, \tag{2.11}$$

where d_i [m] is the mean particle diameter and ρ_i [kg/m^3] is the density for the ith population, $||\mathbf{g}||_2$ [m/s^2] is the gravity magnitude, and ρ_l [kg/m^3] (resp. μ_l [N s/m^2]) is the density (resp. viscosity) of the fluid. The flux (2.10) vanishes at $fs_i = 0$ and $fs = fs_{CR}$, so that the domain $(0, fs_{CR})$ is invariant.

The parabolic flux (2.10) is the most natural choice, as it directly ensures that the solid fractions belong to $(0, fs_{CR})$, with zero fluxes at the extremities of this interval (see, e.g., [19,20]). Other models for settling fluxes can be found in, e.g., [21,22].

Note that here the following effects are not taken into account in the model at this point: the resuspension of sediments, the interactions between populations (e.g. aggregation or collisions), or the solid bed modeling (sediment that lies outside the liquid). However, numerical experiments reported in Section 5 indicate that this model is still sufficient to reproduce various interesting sediment ladden flows.

To summarize, the coupled multiphysics problem consists in finding the time evolution of the position of the volume fraction of liquid φ in the cavity Λ, together with the velocity $\mathbf{v}$, the pressure p, and the sediment solid fraction of each sediment particles population fs_i in the liquid mixture domain only.

3. Time discretization

Let $0 = t^0 < t^1 < t^2 < \ldots < t^N = T$ be a subdivision of the time interval $[0, T]$ and $\tau^n = t^{n+1} - t^n$ the $(n+1)$th time step, $n = 0, 1, 2, \ldots, N-1$, τ denoting the largest time step.

Let φ^n, $\mathbf{v}^n$, p^n, $fs_1^n, \ldots, fs_M^n$, Ω^n be approximations of φ, $\mathbf{v}$, p, fs_1, $\ldots$, fs_M, Ω_t respectively at time t^n. Then the approximations φ^{n+1}, $\mathbf{v}^{n+1}$, p^{n+1}, fs_1^{n+1}, $\ldots$, fs_M^{n+1}, Ω^{n+1} at time t^{n+1} are computed by means of a semi-implicit splitting algorithm, which is illustrated in Fig. 2.

3.1. Diffusion operator

First, a discretized time dependent Stokes problem is solved in Ω^n to obtain a prediction of the velocity $\mathbf{v}^{n+1/2}$ and the pressure p^{n+1} in the liquid domain.

We proceed as follows: the approximations fs_i^n $(i = 1, \ldots, M)$ allow to define respectively approximations $\rho^n = \rho(fs^n)$, $\mu^n = \mu(fs^n)$ and $\alpha^n = \alpha(fs^n)$ of the density $\rho(fs)$, viscosity $\mu(fs)$ and reaction coefficient $\alpha(fs)$ following (2.4)–(2.6). We use the following implicit Euler scheme for the solution of the Stokes equations:

$$\begin{aligned} \rho^n \frac{\mathbf{v}^{n+1/2} - \mathbf{v}^n}{\tau^n} - 2\nabla \cdot \left(\mu^n \mathbf{D}(\mathbf{v}^{n+1/2})\right) \\ + \nabla p^{n+1} + \alpha^n \mathbf{v}^{n+1/2} = \rho^n \mathbf{g} \quad \text{in } \Omega^n, \\ \nabla \cdot \mathbf{v}^{n+1/2} = 0 \qquad \text{in } \Omega^n. \end{aligned} \tag{3.1}$$

with zero force condition on the liquid-air interface $\partial\Omega^n \backslash \partial\Lambda$, and no-slip or pure-slip conditions on the boundary of the cavity Λ.

3.2. Sedimentation deposition operator

Second, in the operator splitting strategy, (2.9) is decoupled into a transport equation (treated in Section 3.3) and a sedimentation deposition operator that describes the vertical deposition (along the gravity field) of the sediments. The deposition step consists in solving between t^n and t^{n+1}:

$$\frac{\partial fs_i}{\partial t} + \nabla \cdot \mathbf{F}(fs_i) = 0, \quad i = 1, \ldots, M, \tag{3.2}$$

together with the initial conditions $fs_i(t^n) = fs_i^n$, $i = 1, \ldots, M$, and set

$$fs_i^{n+1/2} = fs_i(t^{n+1}), \quad i = 1, \ldots, M.$$

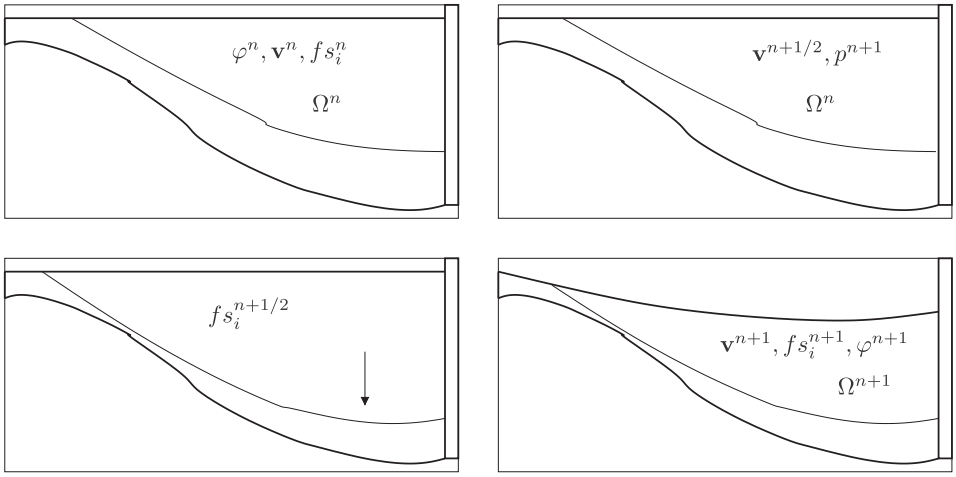

Fig. 2. Operator splitting algorithm (from left to right, top to bottom). At each time step n, we first solve a time dependent Stokes problem to obtain the predicted velocity $\mathbf{v}^{n+1/2}$ and the pressure p^{n+1} in the liquid domain Ω^n. Second, the sediment vertical deposition is computed to obtain predicted concentrations $fs_i^{n+1/2}$, $i = 1, \ldots, M$. Finally, advection problems are solved to determine the new approximation of the characteristic function φ^{n+1} (and thus the new liquid domain Ω^{n+1}), and the corrected velocity $\mathbf{v}^{n+1}$ and concentrations fs_i^{n+1}, $i = 1, \ldots, M$.

It is solved with a classical finite-volume method for conservation laws (see for instance [23]) which is described in Section 4.3.

3.3. Advection operator

Third, the predicted velocity $\mathbf{v}^{n+1/2}$ can be used to transport the volume fraction of liquid φ^n, the solid fractions $fs_i^{n+1/2}$, and the velocity $\mathbf{v}^{n+1/2}$ itself (by considering the convection operator of the Navier–Stokes equations separately). Thus we compute corrections of the velocity $\mathbf{v}^{n+1}$ and solid fractions fs_i^{n+1} defined on a new liquid domain Ω^{n+1} defined thanks to φ^{n+1}. More precisely, this advection step consists in solving, between t^n and t^{n+1} the following system of nonlinear equations:

$$\frac{\partial \varphi}{\partial t} + \mathbf{v} \cdot \nabla \varphi = 0, \tag{3.3}$$

$$\frac{\partial fs_i}{\partial t} + \mathbf{v} \cdot \nabla fs_i = 0, \qquad i = 1, \ldots, M, \tag{3.4}$$

$$\frac{\partial \mathbf{v}}{\partial t} + (\mathbf{v} \cdot \nabla)\mathbf{v} = 0, \tag{3.5}$$

with initial conditions φ^n, $fs_i^{n+1/2}$ and $\mathbf{v}^{n+1/2}$ respectively. This system of hyperbolic equations is linearized and solved with a forward characteristics method, so that φ^{n+1}, fs_i^{n+1} and $\mathbf{v}^{n+1}$ are respectively given by

$$\varphi^{n+1}(\mathbf{x} + \tau^n \mathbf{v}^{n+1/2}(\mathbf{x})) = \varphi^n(\mathbf{x}), \tag{3.6}$$

$$fs_i^{n+1}(\mathbf{x} + \tau^n \mathbf{v}^{n+1/2}(\mathbf{x})) = fs_i^{n+1/2}(\mathbf{x}), \qquad i = 1, \ldots, M, \tag{3.7}$$

$$\mathbf{v}^{n+1}(\mathbf{x} + \tau^n \mathbf{v}^{n+1/2}(\mathbf{x})) = \mathbf{v}^{n+1/2}(\mathbf{x}), \tag{3.8}$$

for all $\mathbf{x} \in \Omega^n$. The new liquid domain Ω^{n+1} is then defined as $\Omega^{n+1} = \{\mathbf{x} \in \Lambda : \varphi^{n+1}(\mathbf{x}) = 1\}$.

4. Space discretization

In order to solve this multiphysics problem, a two-grids method is used, following [11–13,17]. As illustrated in Fig. 3 (in two dimensions of space), a regular grid of small structured cells is used to solve the advection problems (3.6)–(3.8) and the sedimentation problem (3.2), while the solution of the diffusion problem (3.1) is performed on a coarser unstructured tetrahedral finite element mesh. The goal of introducing a two-grid method is to increase the accuracy of the approximation of the free surfaces (by decreasing the numerical diffusion of the approximation φ^{n+1} in (3.6)) and of the solution of the conservation laws, while keeping reasonable the computational cost of solving the Stokes problem. Adaptive techniques for both grids have been investigated in [12,24] but are not discussed here.

Let $\mathcal{T}_H$ be a finite element tetrahedral discretization of the cavity Λ, with typical size H. The cavity Λ is embedded into a parallelipipedic box discretized into a structured Cartesian grid $\mathcal{C}_h$, which is made out of small cells whose dimensions are denoted by (h_x, h_y, h_z), with a typical size $h := \max\{h_x, h_y, h_z\}$. We label each cell by the indices (ijk), and denote by C_{ijk} a generic cell of $\mathcal{C}_h$. Following [17], we typically advocate $H \simeq 3h - 5h$ in the numerical experiments presented hereafter.

4.1. Diffusion operator

Let φ_H^n be the volume fraction of liquid defined by the piecewise linear finite element approximation of φ^n defined by its values at the vertices of $\mathcal{T}_H$. The liquid region Ω_H^n is defined by the union of all tetrahedra of the finite element mesh $\mathcal{T}_H$ having (at least) one of its vertices P with a value $\varphi_P^n > 0.5$.

Let $\mathbf{v}_H^n \in (V_H)^3$ (resp. $p_H^n \in Q_H$) be piecewise polynomial approximations of $\mathbf{v}^n$ (resp. p^n), using the finite element spaces

$$V_H = \left\{ v_H \in C^0(\Lambda) : \ v_H|_K \in \mathbb{P}_1^B, \ \forall K \in \mathcal{T}_H \right\}, \tag{4.1}$$

$$Q_H = \left\{ q_H \in C^0(\Lambda) : \ q_H|_K \in \mathbb{P}_1, \ \forall K \in \mathcal{T}_H \right\}, \tag{4.2}$$

where $\mathbb{P}_1^B$ the classical space of polynomials of first degree on K enriched with a bubble function [25]. Let us define ρ_H^n, μ_H^n and α_H^n the piecewise constant approximations of ρ^n, μ^n and α^n on each tetrahedron, respectively. The Stokes problem is solved with $\mathbb{P}_1^B - \mathbb{P}_1$ finite elements; it consists in finding the velocity $\mathbf{v}_H^{n+1/2} \in (V_H)^3$ and the pressure $p_H^{n+1} \in Q_H$, satisfying the essential boundary conditions on $\partial\Omega_H^n$, and such that:

Please cite this article as: S. Boyaval et al., A semi-Lagrangian splitting method for the numerical simulation of sediment transport with free surface flows, Computers and Fluids (2018), https://doi.org/10.1016/j.compfluid.2018.04.002

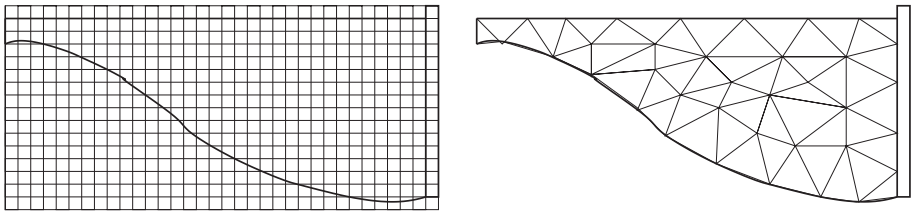

Fig. 3. Two-grid method (2D sketch): the advection problems and the hyperbolic conservation law are solved on a structured grid of small square cells $\mathcal{C}_h$ (left), and the diffusion problem is solved on an unstructured finite element mesh $\mathcal{T}_H$ (right).

$$\int_{\Omega_H^n}\left(\rho_H^n\frac{\mathbf{v}_H^{n+1/2}-\mathbf{v}_H^n}{\tau^n}\cdot\mathbf{w}+2\mu_H^n\mathbf{D}(\mathbf{v}_H^{n+1/2}):\mathbf{D}(\mathbf{w})+\alpha_H^n\mathbf{v}_H^{n+1/2}\cdot\mathbf{w}\right)d\mathbf{x}$$
$$-\int_{\Omega_H^n}p_H^n\nabla\cdot\mathbf{w}d\mathbf{x}-\int_{\Omega_H^n}q\nabla\cdot\mathbf{v}_H^{n+1/2}d\mathbf{x}=\int_{\Omega_H^n}\rho_H^n\mathbf{g}\cdot\mathbf{w}d\mathbf{x}, \quad (4.3)$$

for all $\mathbf{w}$ and q the velocity and pressure test functions, compatible with the essential boundary conditions on $\partial\Omega_H^n$. The corresponding linear system is solved with a sequential preconditioned GMRES method.

4.2. Interpolation on the structured grid

The continuous $\mathbb{P}_1^B$-approximation of the velocity $\mathbf{v}_H^{n+1/2}$ on $\mathcal{T}_H$ is interpolated at the center of each cell C_{ijk} to obtain values $\mathbf{v}_{ijk}^{n+1/2}$ on the structured grid $\mathcal{C}_h$ (i.e. a piecewise constant approximation). When the center of the cell C_{ijk} belongs to the element K, the field is restricted by a *geometric distance-based interpolation*. Denoting by $\mathcal{P}_J$, $J=0,\dots,3$ the vertices of K, by $\mathcal{P}_4$ the barycenter of K, and by $\mathbf{v}_{H,J}^{n+1/2}$ the values of the velocity at point $\mathcal{P}_J$ for $J=0,\dots,4$, we compute a weighted average

$$\mathbf{v}_{ijk}^{n+1/2}=\frac{\sum_{J=0}^4\mathbf{v}_{H,J}^{n+1/2}\,\mathrm{dist}(C_{ijk},\mathcal{P}_J)^{-2}}{\sum_{J=0}^4\mathrm{dist}(C_{ijk},\mathcal{P}_J)^{-2}}, \quad (4.4)$$

where $\mathrm{dist}(\cdot,\cdot)$ denotes the Euclidean distance. A special treatment is applied when the cell center coincides exactly with the location of a degree of freedom in K.

4.3. Sedimentation operator

From now on, and for all numerical experiments presented in Section 5, the gravity $\mathbf{g}$ is assumed to aligned with the Oz axis. Problem (3.2) is therefore an one-dimensional problem, which can be written as an instance of the generic one-dimensional nonlinear conservation law (using $\theta=\theta(z,t)$ as fs_i):

$$\frac{\partial\theta}{\partial t}+\frac{\partial f(\theta)}{\partial z}=0, \quad (4.5)$$

where

$$f(\theta)=-\kappa v_{stokes}\theta\left(1-\frac{\theta}{\theta_{\max}}\right). \quad (4.6)$$

Let us consider one column of elements of $\mathcal{C}_h$, corresponding to the fixed indices (i,j), and denote by θ_{ijk}^n the value of the approximation θ^n in the cell (i,j,k). Let us also note N_Z the number of cells in the z-direction in the column (i,j). We use a time-explicit finite volume method, namely the Godunov scheme, to solve (4.5): for $k=1,\dots,N_Z$, we set $\theta_{ijk}^{n+1/2}$ as

$$\theta_{ijk}^{n+1/2}=\theta_{ijk}^n+\frac{\bar\tau^n}{h_z}\left(F_{ij,k-1/2}-F_{ij,k+1/2}\right), \quad (4.7)$$

where $\bar\tau^n$ is the largest time step such that $\bar\tau^n\le\tau^n$, and $\max_{0<\xi<fs_{CR}}|f'(\xi)|\cdot\bar\tau^n\le h_z$ (potentially determined via sub-iterations), and $F_{ij,k+1/2}$ is the flux between the cells k and $k+1$ given by

$$F_{ij,k+1/2}=\begin{cases}\min\limits_{\theta_{ij,k}^n\le\xi\le\theta_{ij,k+1}^n}f(\xi), & \text{if } \theta_{ij,k}^n\le\theta_{ij,k+1}^n,\\ \max\limits_{\theta_{ij,k+1}^n\le\xi\le\theta_{ij,k}^n}f(\xi), & \text{if } \theta_{ij,k+1}^n\le\theta_{ij,k}^n,\end{cases} \quad (4.8)$$

Relationship (4.8) requires an optimisation problem to be solved between each consequent cells. However, if the flux has a single minimum at a point denoted by ω, and no local maxima within the $]0,fs_{CR}[$ interval (which is the case with (4.6) by convexity), we have the following property:

$$F_{ij,k+1/2}=\max\left(f(\max(\theta_{ij,k}^n,\omega)),f(\min(\theta_{ij,k+1}^n,\omega))\right). \quad (4.9)$$

This relationship allows a fast computation of the fluxes. On the top and bottom of each column, from (4.6), zero flux conditions are imposed, namely $F_{ij,1/2}=F_{ij,N_Z+1/2}=0$. The sedimentation step allows to obtain a prediction $fs_i^{n+1/2}$ of the sediment concentration, which is corrected in the advection step below.

Other fluxes (instead of (4.6)) have been suggested in the literature for the simulation of sediment deposition, e.g. [21,22]. An approximate Riemann solver, such as the one introduced in [26], may have to be considered for those cases.

If the gravity is not aligned with one of the coordinate axis, we have to consider a 3D scalar hyperbolic problem instead of (4.5), and adapt the numerical techniques, for instance by solving two additional flux-differences problem like (4.7), one per additional space dimension.

4.4. Advection operator

Equations (3.6)–(3.8) are implemented on the structured grid $\mathcal{C}_h$, using, at time t^n, constant values within each cell C_{ijk}. More precisely, the algorithm consists in moving the cell (ijk) along $\tau^n\mathbf{v}_{ijk}^{n+1/2}$, and conservatively redistributing the transported quantities, φ_{ijk}^n, $fs_{ijk}^{n+1/2}$ and $\mathbf{v}_{ijk}^{n+1/2}$, into the overlapped cells (proportionally to the volume intersected by the transported cell and the overlapped cells).

In order to enhance the quality of the approximation φ_{ijk}^n of the volume fraction of liquid, and reduce the numerical diffusion, we use a variation of the heuristic SLIC algorithm inspired by Noh and Woodward [27] to reduce the numerical diffusion of the front. Details can be found in [17].

In order to avoid the artificial compression of the fluid and/or of the sediment concentration (i.e. when $\varphi_{ijk}^{n+1}>1$ or $fs_{ijk}^{n+1}>fs_{CR}$ for some (ijk)), a post-processing technique redistributes the excess of liquid and solid fractions from over-filled cells to non-full cells. Related to global repair algorithms [28], this *decompression* technique produces final values φ_{ijk}^{n+1} (resp. fs_{ijk}^{n+1}) which are between zero and one (resp. zero and fs_{CR}). Details can be found in [17].

4.5. Projection on the finite element triangulation $\mathcal{T}_H$

Once values φ_{ijk}^{n+1}, fs_{ijk}^{n+1} and $\mathbf{v}_{ijk}^{n+1}$ have been computed on $\mathcal{C}_h$, the approximated fields are interpolated at the vertices (and pos-

sibly at the barycenter when projecting the velocity) of each tetrahedra K of the mesh $\mathcal{T}_H$, in order to restart the next time step with the Stokes problem. The volume fraction of liquid at the vertex $\mathcal{P}$ is computed by considering all the cells in the tetrahedra that are adjacent with $\mathcal{P}$:

$$\varphi_H^{n+1}(\mathcal{P}) = \frac{\sum_{K,\mathcal{P}\in K}\ \sum_{C_{ijk}\in K} \varphi_{ijk}^{n+1}\cdot \mathrm{dist}(C_{ijk},\mathcal{P})^{-2}}{\sum_{K,\mathcal{P}\in K}\ \sum_{C_{ijk}\in K} \mathrm{dist}(C_{ijk},\mathcal{P})^{-2}}. \tag{4.10}$$

If the point considered is the barycenter of a tetrahedron K, the formula is modified to account only for the element K and not the adjacent tetrahedra.

When the values of φ_H^{n+1} are available at the vertices of $\mathcal{T}_H$, the liquid region Ω_H^{n+1} is defined as follows: an element of the finite element mesh $\mathcal{T}_H$ is said to be *liquid* if (at least) one of its vertices P has a value $\varphi_P^{n+1} > 0.5$. The computational domain Ω_H^{n+1} is defined as the union of all liquid elements.

The approximations ρ_H^{n+1}, μ_H^{n+1} and α_H^{n+1} are computed on the finite element mesh in order to solve (4.3). More precisely, piecewise constant approximations of those quantities are first computed on the structured grid $\mathcal{C}_h$ following (2.4)–(2.6), based on the piecewise constant approximations of the sediment concentrations that are obtained on the grid of cells after the advection step. These values are then interpolated on the finite element mesh to obtain piecewise constant approximations of the physical properties. For instance, the approximation of the density is given by:

$$\rho_H^{n+1}\big|_K = \frac{\sum_{C_{ijk}\in K} \rho_{ijk}^{n+1}\cdot \mathrm{dist}(C_{ijk},\mathcal{B})^{-2}}{\sum_{C_{ijk}\in K} \mathrm{dist}(C_{ijk},\mathcal{B})^{-2}}, \tag{4.11}$$

where $\mathcal{B}$ is the barycentric center of element K. Similar relationships apply for μ_H^{n+1} and α_H^{n+1}, to obtain piecewise constant approximations of those quantities on the finite element mesh $\mathcal{T}_H$.

Under the CFL condition ($\frac{\max||\mathbf{v}_H||_2\,\tau}{h} \le C_{CFL}$), and provided that $H \simeq 3h - 5h$, the overall convergence rate of the numerical method is order one. Thus, when dividing H, h and τ by two, the error should be divided by two.

5. Numerical experiments

Numerical experiments are detailed in the sequel to validate the numerical approach, to benchmark the computational results with experiments, and to discuss the limits of the underlying physical models.

5.1. Sedimentation of polystyrene particles in a still fluid

The goal of the first experiment is to validate the numerical treatment of the sediment operator in the multiphysics problem, and confirm the convergence of the method when the discretization parameters tend to zero.

In order to do so, let us consider the sedimentation of suspended, mono disperse ($M = 1$), polystyrene particles in a tank of silicon oil. The particles properties are $d_* = 290$ [μm] and $\rho_p = 1.05$ [g cm^{-3}]; the silicon oil has $\mu_l = 0.02$ [Pa s] and $\rho_l = 0.95$ [g cm^{-3}]. The dimensions of the tank are $2.5 \times 0.05 \times 10$ [cm^3]. A mixing procedure was used to obtain a well-mixed, very dense, liquid mixture of uniform distribution $fs(0) = 0.48$ in the bottom half of the domain ($z \le 5.55$ [cm]). The maximal solid fraction is $fs_{CR} = 0.6$, the cohesion parameter is $fs_{CO} = 0.5999$, $\varepsilon = 0.4$, and $K = 1$.

This sedimentation process has been investigated in [21] with a comparison between a 1D model and experimental results, and in [29] with a multiphase 2D model.

If we consider the parabolic flux (2.10), and the corresponding analytical prototypical problem for $\theta \in (0, \theta_{\max})$,

$$\frac{\partial\theta}{\partial t} + \frac{\partial}{\partial z}(\alpha\theta(\theta - \theta_{\max})) = 0, \qquad \text{in} \quad \mathbb{R},$$

with $\alpha = \kappa v_{stokes}/\theta_{\max}$, $\theta_{\max} = fs_{CR}$, and with a discontinuous initial solution that reads:

$$\theta(t=0) = \begin{cases} \theta_+ = 0, & z \ge 0 = z_0 \\ \theta_- = 0.48, & 0 \ge z \ge z^- \\ \theta_{\max} = 0.6, & z^- \ge z. \end{cases}$$

In such case, an analytical solution can be obtained explicitly, and we obtain the development of two shockwaves, with shock speeds respectively equal to -0.12 and $+0.48$. The intersection of the two shocks takes place at $(t^\star, z^\star)$, with

$$z^\star = z^- + \alpha 0.48 t^\star = \alpha(-0.12)t^\star,$$

which leads to $(t^\star, z^\star) = (1084.0, 0.044)$ in the case of this particular experiment.

Fig. 4 shows the snapshots of the sediment concentration at different times for our model with the parabolic flux ($\kappa = 1$). The numerical results show indeed the evolution of the two interfaces: one that separates the clear fluid and the mixed fluid and another one between the mixed fluid and the fluid saturated with sediments. Fig. 5 illustrates the positions of these interfaces with, in particular: i) a comparison with [29], in which experimental data and simulations are compared with a 2D multiphase model, ii) a comparison with the analytical solution derived previously, and iii) the evolution of the positions of these interfaces when the discretization parameters tends to zero. For the convergence study, we consider three discretizations, respectively, with: (i) $H = 0.006638$, $h = 0.001$, and $\tau = 0.01$ [s] (so-called coarse mesh); (ii) $H = 0.004978$, $h = 0.00075$, and $\tau = 0.0075$ [s] (intermediate mesh); and (iii) $H = 0.003319$, $h = 0.0005$, and $\tau = 0.005$ [s] (fine mesh). These results show not only a very good agreement of the computational results with existing ones, but also the convergence of the method when the discretization parameters tends to zero.

In order to quantitatively assess the convergence of the approximated solutions, we define two error estimates. The first estimate is based on the approximation error on the time trajectories of the interfaces (and the final time); the second is based on the L^1 error on the solution of the hyperbolic equation. Namely:

$$E_1 = ||z_1 - z_{1h}||_{L^2(0,t^\star)} + ||z_2 - z_{2h}||_{L^2(0,t^\star)} + |t^\star - t_h|,$$
$$E_2 = ||fs - fs_h||_{L^1(\Lambda)},$$

where $z_1(t) = z^- + \alpha 0.48 t$ (resp. $z_2(t) = \alpha(-0.12)t$) denote the time evolution of the lower and upper interfaces, z_{1h}, z_{2h} their respective numerical approximations, and $t^\star$ the exact time of intersection of the two trajectories. The position of the interfaces $z_{1\mathrm{h}}(t)$ and $z_{2\mathrm{h}}(t)$ are computed on the grid $\mathcal{C}_h$ as follows. The position $z_{1\mathrm{h}}(t)$ is given by the vertical position of the center of the first cell (swept from bottom to top) such that $fs_{ijk}^{n+1} > fs_{CR} - \varepsilon_P$, where $\varepsilon_P = 10^{-5}$. Reciprocally, the position $z_2\mathrm{h}(t)$ is given by the vertical position of the first cell (swept from top to bottom) such that $fs_{ijk}^{n+1} < \varepsilon_P$. Fig. 6 illustrates the convergence of these estimates when the discretization parameters h, H and τ tend to zero, and shows an appropriate first order convergence order.

5.2. Erosion by an impinging liquid jet

In order to validate the numerical algorithm for the multiphysics model, we consider the benchmark simulation of the erosion of a immersed granular bed by an impinging liquid jet perpendicular to the surface of the consolidated sediment. We consider this erosion process as described in [30,31]. The experiment consists of a bed load of non-cohesive sediments, initially at rest at the bottom of a parallelipidedic domain of size $0.495 \times 0.032 \times 0.2$ [m^3], as illustrated in Fig. 7.

The bed load on non-cohesive sediment is composed by sand (with particles of diameter $4.0 \cdot 10^{-4}$ [m]); the dry density of the sand particles is 2500 [kg m^{-3}], while the bulk density is that

Please cite this article as: S. Boyaval et al., A semi-Lagrangian splitting method for the numerical simulation of sediment transport with free surface flows, Computers and Fluids (2018), https://doi.org/10.1016/j.compfluid.2018.04.002

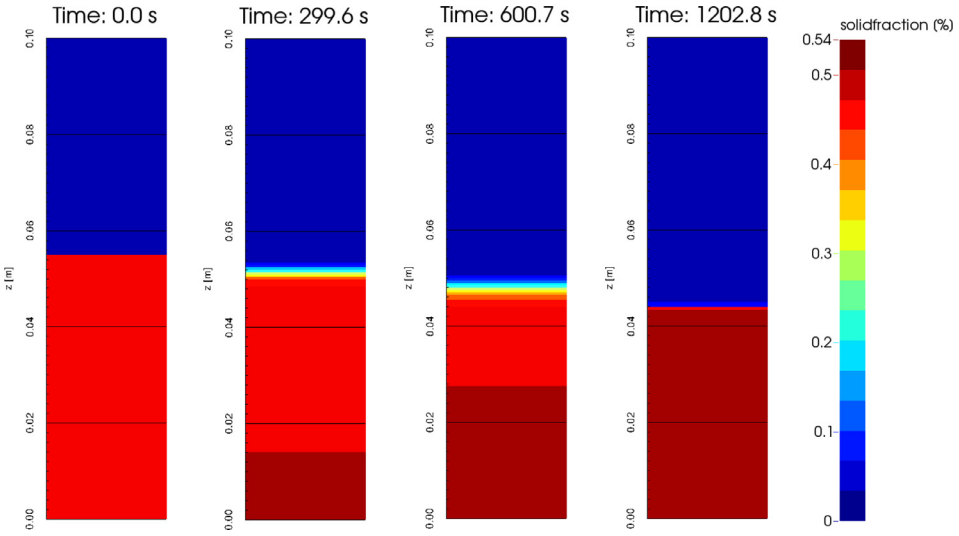

Fig. 4. Numerical simulation of the sedimentation of polystyrene particles. Snapshots of the solid fraction *fs*.

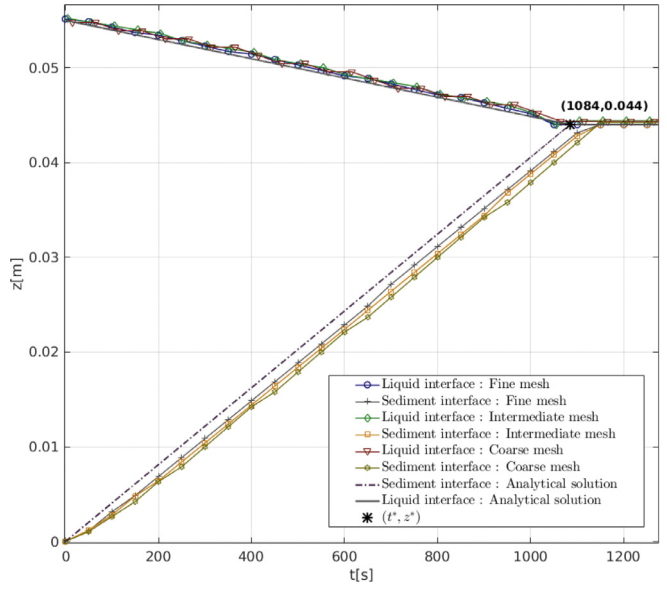

Fig. 5. Numerical simulation of the sedimentation of polystyrene particles. Time evolution of the two interfaces, including i) a comparison with [29] – experimental and numerical data –, ii) a comparison with the analytical solution, and iii) a convergence study when the discretization parameters tends to zero.

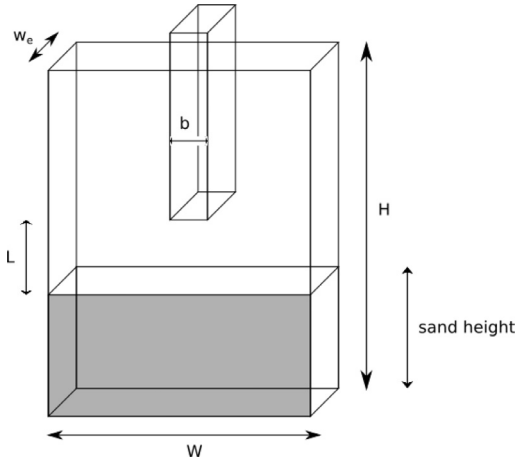

Fig. 7. Erosion by an impinging liquid jet. Sketch of the geometrical domain and numerical setup.

of water, i.e. 1000 [kg m^{-3}]. The computational domain is actually smaller than the physical domain, and formed by a parallelipidedic domain of size $0.2 \times 0.004 \times 0.135$ [m^3]. The initial conditions consist of a domain entirely filled with liquid. The sediment concentration is maximal (i.e. $fs_{CR} = 0.63$) when $z \leq 0.05$ [m] and zero otherwise. The water is vertically injected on the top of the do-

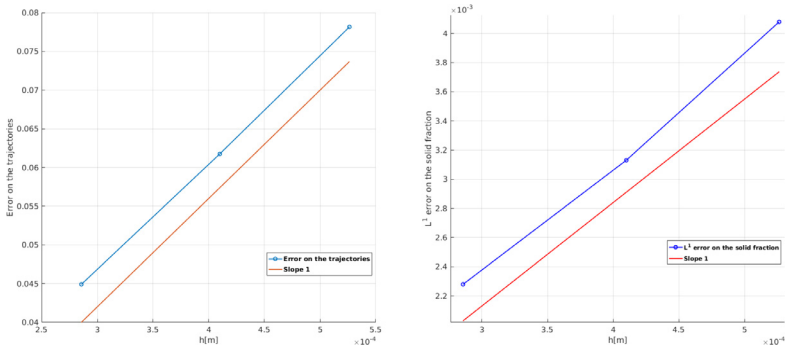

Fig. 6. Numerical simulation of the sedimentation of polystyrene particles. Convergence study when the discretization parameters tends to zero. Convergence of the error estimates E_1 (left) and E_2 (right) when $h \to 0$.

Please cite this article as: S. Boyaval et al., A semi-Lagrangian splitting method for the numerical simulation of sediment transport with free surface flows, Computers and Fluids (2018), https://doi.org/10.1016/j.compfluid.2018.04.002

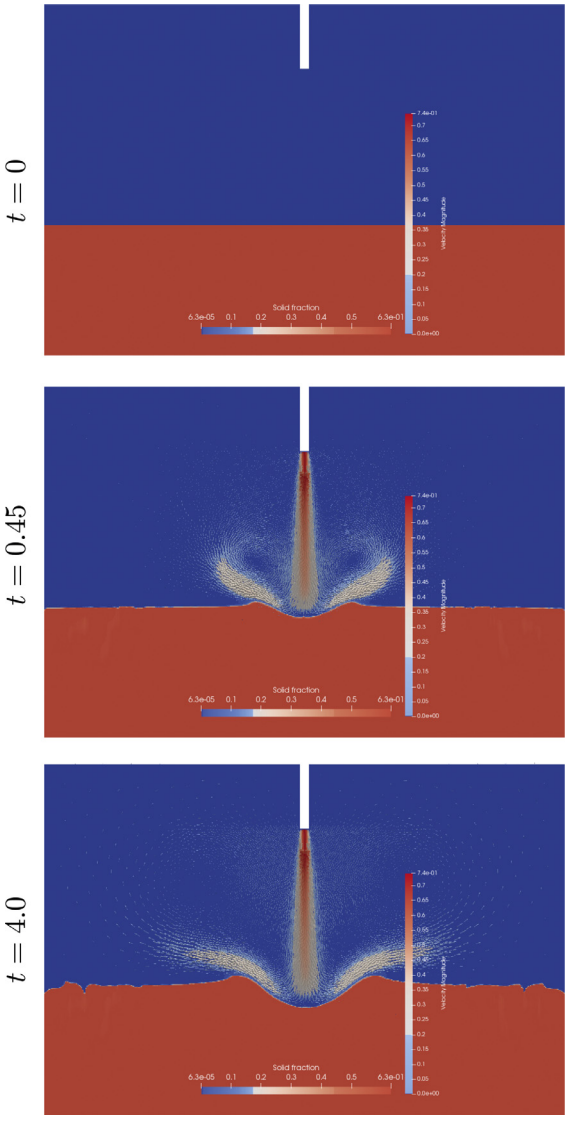

Fig. 8. Erosion by an impinging liquid jet. Snapshots of the numerical solution (sediment position and velocity field) at times $t = 0, 0.45$ and 4.0 [s].

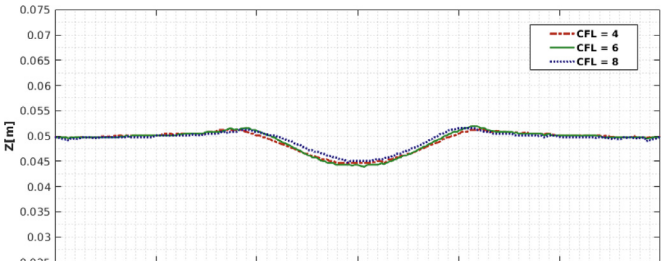

Fig. 9. Erosion by an impinging liquid jet. Determination of the optimal time step via the CFL criterion.

main with a velocity following a Poiseuille profile $1.85 \cdot 10^5 (x - 0.102)(x - 0.098)$ [m/s], on the inlet of size 0.004×0.004 [m^2] (so that the maximal velocity is $7.4 \cdot 10^{-1}$ [m/s]). This corresponds to a Reynolds number of $Re \simeq 630$, where $Re = \frac{\rho_l U_J b}{\mu_l}$, and U_J denotes the mean velocity of the inflow velocity, b is the diameter of the injection tube, and μ_l (resp. ρ_l) is the pure water viscosity (resp. density). The liquid can exit at the top of the domain (to compensate for the liquid injected), so that the domain is full at all times. The boundary conditions on the remaining part of the boundary of the domain are homogeneous Dirichlet boundary conditions, except for slip boundary conditions on the lateral walls. The water jet erodes the sand bed to create a hole of width D and depth H. This numerical experiment is used to study the properties of the algorithm, to validate the mesh convergence of the algorithm, and to calibrate the numerical parameters of the model. Fig. 8 illustrates snapshots of the solution, in particular the sediment profile at various times, and illustrates the stationary regime of the flow velocity.

First, let us consider the grids containing 267,520 finite elements and 48,132 vertices in $\mathcal{T}_H$, and 1,071,360 cubic cells in $\mathcal{C}_h$, and obtain the appropriate value of the time step. The value of the time step allows to define a CFL number for the simulation that both allows to maintain stability conditions, and is large enough to minimize the computational effort. Numerical experiments have shown that a CFL number equal to 6 ($\tau = 0.003$ [s]) is appropriate to balance those effects; Fig. 9 illustrates that this value is the value that provides a less diffusive solution.

Fig. 10 shows the time evolution of the depth H and width D of the eroded hole respectively, and confirms that the erosion process has reached a stationary state after roughly $T = 6$ [s], time suitable for all the simulations in the sequel.

In order to study the convergence of the solution when the discretization parameters tend to zero, we consider three discretizations, respectively, with: (i) 157,052 finite elements and 28,115 vertices in $\mathcal{T}_H$ ($H = 0.00135$), and 634,880 cubic cells in $\mathcal{C}_h$ ($h = 0.00054$), $\tau = 0.01$ [s] (so-called coarse mesh); (ii) 490,866 finite elements and 86,051 vertices in $\mathcal{T}_H$ ($H = 0.0009$), and 2,142,720 cubic cells in $\mathcal{C}_h$ ($h = 0.00036$), $\tau = 0.006$ [s] (intermediate mesh); and (iii) 1,133,868 finite elements and 196,506 vertices in $\mathcal{T}_H$ ($H = 0.000675$), and 5,079,040 cubic cells in $\mathcal{C}_h$ ($h = 0.00027$), $\tau = 0.005$ [s] (fine mesh). Fig. 11 illustrates the profile of the water-sand interface after $T = 0.8$ [s], and shows that convergence of the numerical approximations is reached when the mesh sizes tend to zero.

From now on, we consider the intermediate mesh and proceed to the calibration of the parameters involved in the model. Namely, the calibration of the model relies on determining the values of the numerical parameters ε (the regularization parameter in the Carman-Kozeny coefficient), and fs_{CO} (the cohesion threshold). Numerical experiments have shown that optimal values are given by $\varepsilon = 10^{-9}$ and $fs_{CO} = 0.62$ (with $fs_{CR} = 0.63$). The choice of these values is based on the best fit with experiments provided in [30,31], as illustrated in the sequel for these optimal values.

The numerical results obtained with the proposed method are compared with experimental results from [30,31]. Fig. 12 illustrates the values of the width D and depth H of the eroded hole as a function of the inlet velocity magnitude. The results are presented in the same fashion as in [31], namely by expressing the normalized quantities $(D/(L - \lambda)$ and $H/(L - \lambda)$, where $\lambda = 10b$ is a suggested correction of the distance L between the inlet and the sand interface), as a function of the erosion number E_c (defined as $E_c = U_J(b/(L - \lambda))^{1/2}((\frac{\rho_s}{\rho_l} - 1)||\mathbf{g}||_2 d_*)^{-1/2}$). In agreement with [31], we consider inflow velocities inducing Reynolds numbers between $Re = 630$ and $Re = 1890$. Results in Fig. 12 (first row) show that the higher the Reynolds number, the deeper and wider the eroded hole. The regression lines $D/(L - \lambda) = 0.55 + 1.4(E - 1)$ and $H/(L - \lambda) = 0.7(E - 1)$, which are illustrated on the figures, are extracted from [31], compare well with the computational results, and validated our approach for such experiments. The second row of Fig. 12 show the same result when $\lambda = 5b$ is taken as the correction factor, which shows the sensitivity of the post-processed results with respect to post-processing choices.

Please cite this article as: S. Boyaval et al., A semi-Lagrangian splitting method for the numerical simulation of sediment transport with free surface flows, Computers and Fluids (2018), https://doi.org/10.1016/j.compfluid.2018.04.002

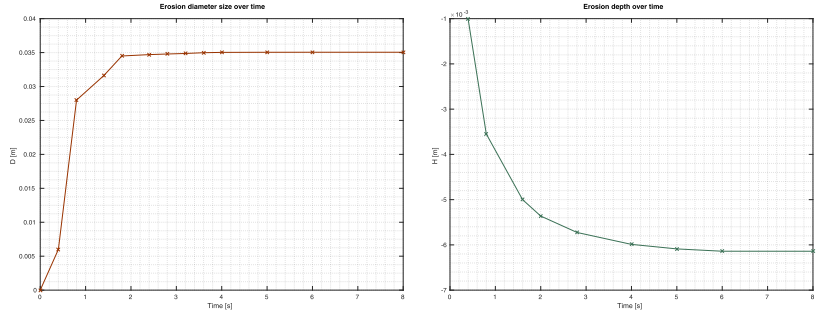

Fig. 10. Erosion by an impinging liquid jet. Left: time evolution of the numerical approximation of the hole width D. Right: time evolution of the numerical approximation of the hole depth H.

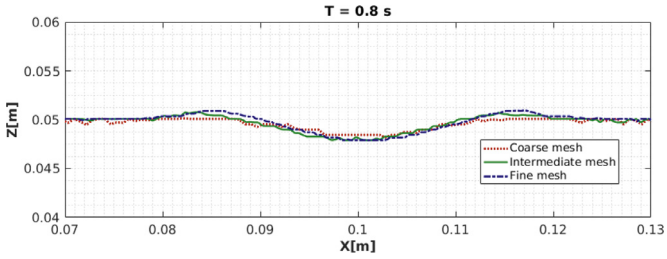

Fig. 11. Erosion by an impinging liquid jet. Convergence of the approximated solution when the discretization parameters tend to zero. Illustration of the sediment-water interface.

5.3. Plunge pool scour

The second experiment is the time evolution of plunge pool scour, caused by an inclined impinging jet of water on a sediments bed. The impact of the inclined jet into the sediments creates a pool scour and a ridge with the transported sediments. As highlighted in [32–34], such jets provoke turbulence in the flow, but eventually converge to steady state conditions for the scour depth and ridge height. Experimental results have been presented in [33,34], while simulations with Flow-3D have been validated in [32].

We consider the full 3D numerical setup used in [32] and illustrated in Fig. 13. The experiment consists of a bed load of non-cohesive sediments, initially at rest at the bottom of a parallelipidedic domain of size $W \times w_e \times L = 1.9 \times 0.5 \times 0.65$ [m^3]. Let us consider three discretizations: the fine one contains 76,380 finite elements and 13,549 vertices in $\mathcal{T}_H$, and 1,267,200 cubic cells in $\mathcal{C}_h$, with $\tau = 0.0085$ [s] (while the intermediate one contains 689,920 cubic cells, with $\tau = 0.01$ [s], and the coarse one contains 483,840 cubic cells, with $\tau = 0.012$ [s]).

The bed load on non-cohesive sediment is composed by nearly uniform particles of diameter $d_* = 0.00125$ [m]; the dry density of the particles is $\rho_s = 1400$ [kg m^{-3}], while the bulk density is that of water, i.e. $\rho_l = 1000$ [kg m^{-3}]. The initial conditions consist of a

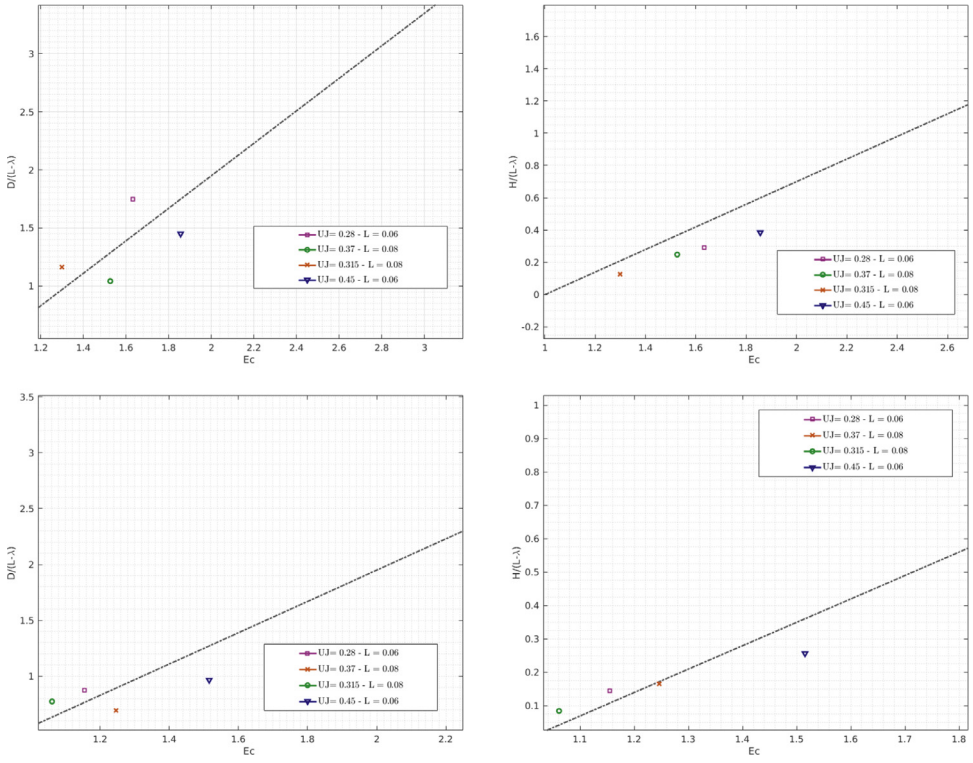

Fig. 12. Erosion by an impinging liquid jet. Numerical approximation of the width D and depth H of the eroded hole, as a function of the inlet velocity magnitude; the regression lines are extracted from [31]. First row : $\lambda = 10b$; second row: $\lambda = 5b$.

Please cite this article as: S. Boyaval et al., A semi-Lagrangian splitting method for the numerical simulation of sediment transport with free surface flows, Computers and Fluids (2018), https://doi.org/10.1016/j.compfluid.2018.04.002

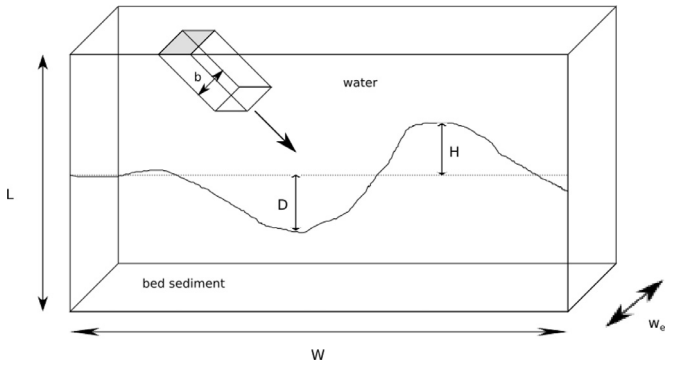

Fig. 13. Plunge pool scour by an inclined impinging liquid jet. Sketch of the geometrical domain and numerical setup.

domain entirely filled with liquid, with zero velocity. The sediment concentration is maximal (i.e. $fs_{CR} = 0.6$) when $z \leq 0.3$ [m] and zero otherwise. The cohesion threshold is given by $fs_{CO} = 0.59$, and $\varepsilon = 10^{-9}$.

The water is injected from the top of the domain with a jet diameter $b = 0.035$ [m] and a jet impact angle $\alpha = 45^{\circ}$. The jet discharge Q is 3.5 [L/s]. This results in a diagonally injected water jet with velocity $\mathbf{u}_{in} = (4.04,\ 0,\ -4.04)^T$ [m/s]. The water level h_0 is kept such that the tail water ratio $T = \frac{h_0}{b}$ is equal to 5.9.

The boundary conditions on the remaining part of the boundary of the domain are homogeneous Dirichlet boundary conditions, except for slip boundary conditions on the symmetry wall. We introduce the dimensionless time $\tau = (g'd)^{\frac{1}{2}}(t/b)$ where t denotes the time [s] and $g' = ||\mathbf{g}||_2(\rho_s - \rho_l)/\rho_l$ denotes the reduced gravitational acceleration. Computational restrictions being inevitable, the end of the calculations is not that of the experiments. It is, however, whenever the steady state of the scour characteristics is observed.

Fig. 14 illustrates snapshots of the solution obtained with the intermediate mesh, in particular the sediment profile at various times. The scour depth D and the nearby ridge H are developing until a state where they only vary in minor orders after about 40 [s]. Fig. 15 illustrates the time evolution of the stationary dimensionless depth $D_d = D/b$, and the dimensionless ridge height $H_d = H/b$, as a function of the dimensionless time τ. Results are post-processed as in [32], and compared with experimental results. We observe that, albeit some numerical diffusion appears (especially for coarser meshes, which is not surprising for 3D calculations), the slope of the graph is adequately reproduced; furthermore, the numerical results improve when the mesh discretization parameters tend to zero.

5.4. Flume bi-disperse gravity currents

In order to validate our numerical method with poly-disperse sediments, we consider a *miscible flume lock-exchange* experiment considered in [35]. It consists of increasing the density of a fluid with a fixed volume of fine silicon carbide particles. This fluid is then released into clear water by removing a separating lock gate. The dimensions of the glass tank are 5.7 [m] long and 0.2 [m] wide; it is filled up to a water height of 0.4 [m], as illustrated in Fig. 16.

In this experiment we consider two ($M = 2$) populations of particles with different sizes, both with density $\rho_i = 3217$ [kg m^{-3}], but with average particle diameters of 25 and 69 [μm] respectively. In all numerical and practical experiments, the total mass of particles is equal to 180 [g], initially suspended in 16 [l] of water. Seven experiments are considered, the proportions of coarse and fine particles varying as specified in Table 1.

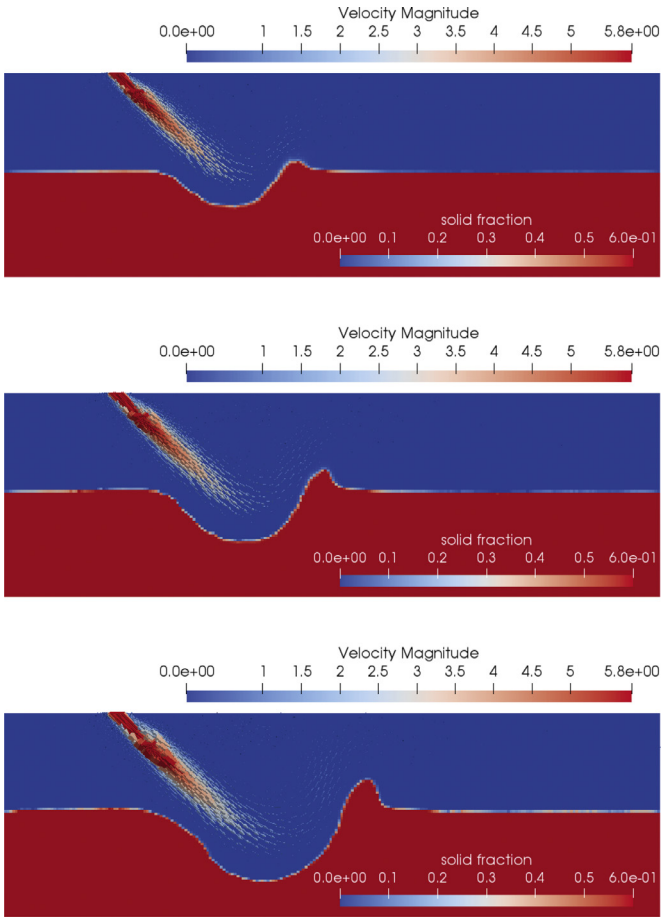

Fig. 14. Plunge pool scour by an inclined impinging liquid jet. Snapshots of the numerical solution (sediment position and velocity field) at times $t = 5$, 10 and 30 [s] (top to bottom).

Table 1
Flume bi-disperse lock-exchange experiment: composition (repartition of sediments between coarse and fine particles) of the sand mixture for the seven experiments, labeled A through G [35].

Experiment	A	B	C	D	E	F	G
% coarse (69 μm)	0	20	40	50	60	80	100
% fine (25 μm)	100	80	60	50	40	20	0

This experiment is a pseudo-2D experiment; compared to [35], the domain is reduced here to a width of 0.02 [cm] along the Oy direction for computational purposes (the dimensions in Ox and Oz directions remain unchanged). The upper free-surface between water and air is not considered and pure slip boundary conditions are applied instead at the top boundary of the domain.

Simulations are performed on a (relatively coarse) discretization ($H = 20$ [mm], $h = 4$ [mm], 53,740 tetrahedra in the finite element mesh and 142,500 cells in the structured grid). Numerical experiments are compared with experiments reported in [35], for various configurations of CFL and boundary conditions. In particular, we compare the sediment front evolution between dense and light miscible liquids (see also [9] for a similar approach for a lock-exchange experiment when the two liquids are immiscible). The time step is adapted automatically to ensure that the CFL condition $\frac{\max||\mathbf{v}_H||_2\,\tau}{h} \leq C_{CFL}$ (where C_{CFL} is a given threshold – so-called *CFL number*) is satisfied.

The experimentalists wait at least 450 [s] to ensure that the deposition of all particles is achieved. When using the characteristics method for the advection of the velocity, one has to consider large

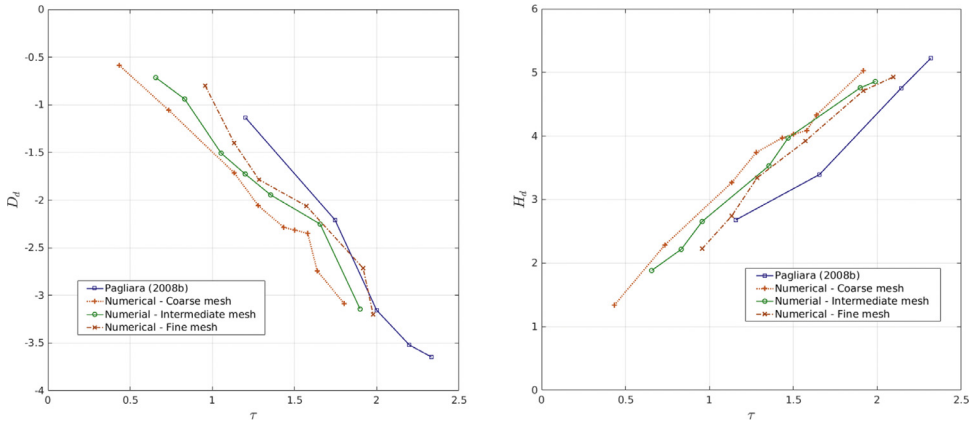

Fig. 15. Plunge pool scour by an inclined impinging liquid jet. Comparison of the time evolution of dimensionless ridge height H_d and scour depth D_d derived from the experiments and those derived from numerical calculations for a coarse, intermediate, and fine meshes.

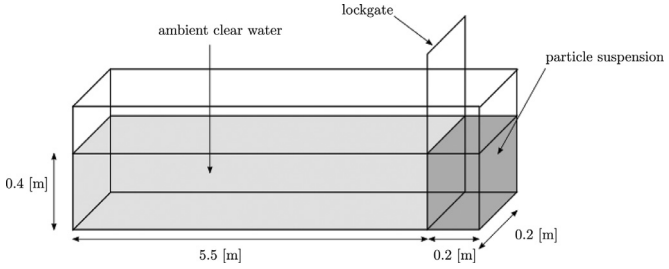

Fig. 16. Flume bi-disperse lock-exchange experiment: setup and dimensions.

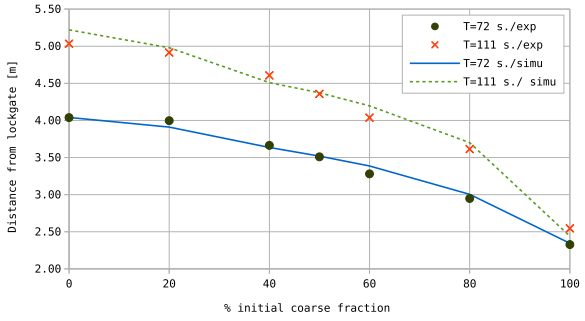

Fig. 17. Flume bi-disperse lock-exchange experiment: comparison of experimental and numerical results. Illustration of the relationship between the distance reached by the particles and the grain size, at two given times $T = 72$ [s] and $T = 111$ [s].

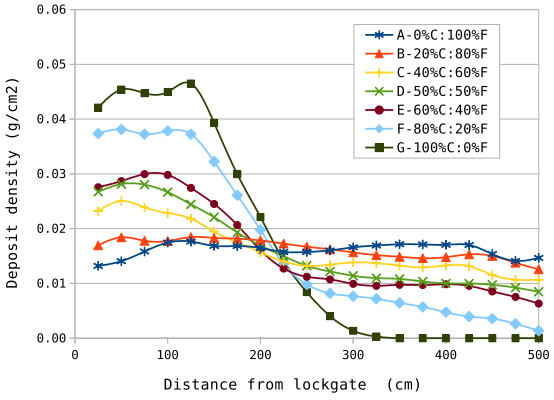

Fig. 18. Flume bi-disperse lock-exchange experiment: simulation results. Relationship between the distance reached by the particles and the total deposit density.

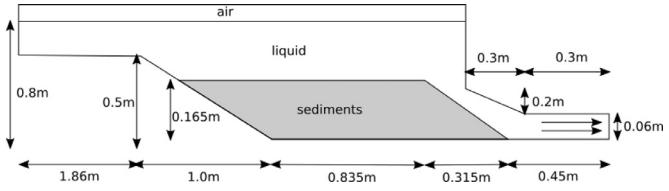

Fig. 19. Flushing of sediments. Sketch of the geometrical domain and numerical setup (similar as in [36]).

CFL numbers ($C_{CFL} \simeq 3 - 6$ numerically), and thus large time steps, to guarantee the efficiency and accuracy of the method over this time frame [17,24].

Simulations have been achieved with the adjusted parabolic sedimentation flux. Fig. 17 represents the computed location of the sediment flow front reached at fixed times, which compares very well with measurements from [35]. According to simulation results, the dependency of the flow velocity upon grain size is strongly nonlinear.

A comparison of the deposit density is illustrated in Fig. 18; it shows the *total deposit density* (for fine and coarse particles), quantified by the concentration of particles on the boundary of the tank after 450 [s] of simulation for all experiments. The general trends and orders of magnitude are accurately tracked, and compare well with the corresponding graph from [35].

5.5. Sediments flushing

We discuss a last numerical experiment, in order to define the range of capability of the physical model, but also illustrate its limitations. We consider a flushing process as described in [36] (and references therein). The importance of flushing techniques has been described, e.g., in [37], for both industrial applications in dams, and natural configurations in rivers and lakes. The experiment consists of a bed load of non-cohesive sediments, initially at rest at the bottom of a channel, as illustrated in Fig. 19. It is realized in a laboratory flume of width 0.2 [m]. The bed load of non-cohesive sediment is composed by sand (with particles of diameter $d_* = 7.6 \cdot 10^{-4}$ [m]); the dry density of the sand particles is $\rho_s = 2650$ [kg m^{-3}], while the bulk density is $\rho_l = 1750$ [kg m^{-3}]. Under vertical gravity forces, the liquid flows out of the domain via the valve on the right, and the sediment is flushed by the rapid flow.

Please cite this article as: S. Boyaval et al., A semi-Lagrangian splitting method for the numerical simulation of sediment transport with free surface flows, Computers and Fluids (2018), https://doi.org/10.1016/j.compfluid.2018.04.002

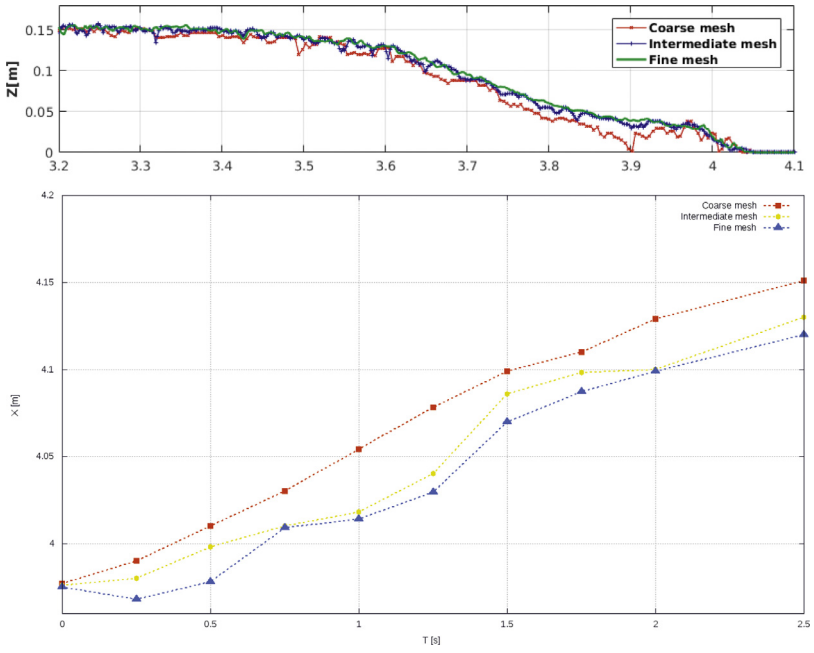

Fig. 20. Sediments flushing. Convergence of the numerical solution when discretization parameters tend to zero. Top: sediment profiles at time $T = 2.5$ [s] for various mesh sizes. Bottom: time evolution of the position of the sediment front.

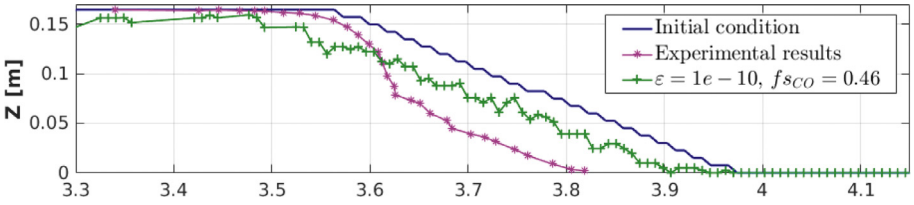

Fig. 21. Sediments flushing. Comparison of sediments profiles at time $T = 48.0$ [s] between the computed solution and the experimental results from [36].

No inflow condition are enforced, but an outflow condition, by imposing a discharge of $q_0 = 0.0079$ [m^3/s] on the bottom right part of the domain (which corresponds to an outflow velocity of 0.132 [m/s]). A free surface between liquid and air lies at the top of the domain, such that the domain is initially full but the liquid level decreases as liquid escapes. Slip boundary conditions are imposed everywhere else. Initially the liquid and sediments are at rest.

We first evaluate the convergence of the numerical method, when the discretization parameters (time step and mesh size) decrease. In order to do so, we run a simulation over 2.5 [s]. We consider three discretizations: (i) 5592 elements/1,144 nodes/646,800 cells, (ii) 32,710 elements/6,237 nodes/5,174,400 cells, and (iii) 218,554 elements/39,430 nodes/41,395,200 cells), with corresponding time steps $\tau = 0.01, 0.003, 0.001$ [s] respectively. Fig. 20 shows the convergence of the solution when the time step and mesh sizes decrease. The top figure illustrates the sediment profile after $T = 2.5$ [s] for the three meshes, while the bottom figure visualizes the position of the sediment front (position of the first particle of sand flushed to the right) for the three meshes. Based on both figures, numerical experiments show convergence of the numerical solution, for both the sediment profile and the position of the front, when the discretization parameters tend to zero.

In a second step, numerical results are compared with experimental results in [36]. We extend the simulation until $T = 48.0$ [s]. Fig. 21 illustrates a comparison between computed and measured sediment profiles. Computed results do not provide profiles with exactly the same slope for the sediment bed as that of experimental results. We infer that this difference comes from the limited physical model considered here, which does not include the resuspension effects of the sediments in the liquid. These effects have been highlighted in [36], when considering the so-called Shields model, and have been deemed to be necessary to match experimental results.

6. Conclusion and perspectives

A three-dimensional numerical model for the transport and sedimentation of poly-dispersed particle populations within a Newtonian flow with free surfaces has been designed. The operator splitting strategy, and the appropriate mix of finite elements, finite volumes and structured grids, has proved to be very flexible to incorporate various numerical solvers. The model has been calibrated versus experiments; the numerical results agree with experimental measurements for pure sedimentation, erosion processes and impinging jets. However, a more complete physical model for the sediments resuspension is missing to adequately model flushing experiments for instance. Future perspectives will thus include the extension of the model with more complete physical components such as re-suspension of cohesive particle bed, the introduction of interactions between populations, and the simulation of real-life 3D topographies.

Acknowledgments

The authors acknowledge the partial support of the Commission for technology and innovation (CTI grant 14359.1 PFES-ES, supporting G. Steiner), the Germaine De Stael program (grant 2016-07,

supporting A. Caboussat), and the ANR (project ANR-15-CE01-0013, supporting S. Boyaval). All the computations were performed using the industrial cfsFlow++ software developed by EPFL and Ycoor Systems SA. The authors thank Alexandre Masserey and Julien Hess (Ycoor Systems SA) for fruitful discussions, and the anonymous referees for their constructive comments.

References

[1] Boillat J-L, Pougatsch H. State of the art of sediment management in Switzerland. In: Proceedings international workshop and symposium on reservoir sedimentation management; 2000. p. 35–45.
[2] Chauchat J, Médale M. A three-dimensional numerical model for incompressible two-phase flow of a granular bed submitted to a laminar shearing flow. Comp Meth App Mech Eng 2010;199(9–12):439–49.
[3] Nguyen DH, Levy F, Bang DPV, Guillou S, Nguyen KD, Chauchat J. Simulation of dredged sediment releases into homogeneous water using a two-phase model. Adv Water Resour 2012;48:102–12.
[4] Ruiz R, Lunati I. Mixed finite element – discontinuous finite volume element discretization of a general class of multicontinuum models. J Comput Phys 2016;322:666–88.
[5] Golay F, Lachouette D, Bonelli S, Seppecher P. Interfacial erosion: a three-dimensional numerical model. C R Mecanique 2010;338(6):333–7.
[6] Lachouette D, Bonelli S, Golay F, Seppecher P. Numerical modelling of soil interface erosion. Comp Meth App Mech Eng 2011;200(1–4):383–91.
[7] Ferguson RI, Church M. A simple universal equation for grain settling velocity. J Sedimentary Res 2004;74(6):933–7.
[8] Lyn DA. Resistance in flat-bed sediment-laden flows. J Hydraul Eng 1991;117(94–114).
[9] James N, Caboussat A, Boyaval S, Picasso M. Numerical simulation of 3D free surface flows, with multiple incompressible immiscible phases. Applications to impulse waves. Int J Numer Methods Fluids 2014;00:1–24.
[10] Bonito A, Caboussat A, Picasso M, Rappaz J. A numerical method for fluid flows with complex free surfaces. In: Glowinski R, Neittaanmäki P, editors. Partial differential equations. Computational Methods in Applied Sciences, 16. Springer Netherlands; 2008. p. 187–208.
[11] Caboussat A. A numerical method for the simulation of free surface flows with surface tension. Comput Fluids 2006;35(10):1205–16.
[12] Caboussat A, Clausen P, Rappaz J. Numerical simulation of two-phase flow with interface tracking by adaptive Eulerian grid subdivision. Math Comput Modell 2012;55:490–504.
[13] Caboussat A, Picasso M, Rappaz J. Numerical simulation of free surface incompressible liquid flows surrounded by compressible gas. J Comput Phys 2005;203(2):626–49.
[14] Caboussat A, Boyaval S, Masserey A. On the modeling and simulation of non-hydrostatic dam break flows. Comput Vis Sci 2013;14(8):401–17.
[15] Alvarez M, Gatica GN, Ruiz R. A posteriori error analysis of a fully-mixed formulation for the Brinkman–Darcy problem. Calcolo 2017;54(4):1491–519.
[16] Brinkman HC. A calculation of the viscous force exerted by a flowing fluid on a dense swarm of particles. Appl Sci Res 1949;1:27–34.
[17] Maronnier V, Picasso M, Rappaz J. Numerical simulation of three dimensional free surface flows. Int J Num Meth Fluids 2003;42(7):697–716.
[18] Ishii M, Zuber N. Drag coefficient and relative velocity in bubbly, droplet or particulate flows. AIChE J 1979;25(5):843–55. doi:10.1002/aic.690250513.
[19] Concha F, Bustos MC. Settling velocities of particulate systems, 6. Kynch sedimentation processes : batch settling. Int J Miner Process 1991;32:193–212.
[20] Kynch GJ. A theory of sedimentation. Trans Faraday Soc 1952;48:166–76.
[21] Bang DPV, Lefrançois E, Ovarlez G, Bertrand F. MRI experimental and 1D FE-FCT numerical investigation of the sedimentation and consolidation. In: Seventh international conference on hydroinformatics, 1; 2006. p. 497–504.
[22] Ungarish M. On the modeling and investigation of polydispersed rotating suspensions. Int J Multiphase Flow 1995;21:262–84.
[23] LeVeque RJ. Numerical methods for conservation laws. ETH Zurich: Birkhaüser-Verlag; 1990.
[24] Laurmaa V, Picasso M, Steiner G. An octree-based adaptive semi-Lagrangian VOF approach for simulating the displacement of free surfaces. Comput Fluids 2016;131:190–204.
[25] Arnold D, Brezzi F, Fortin M. A stable finite element for the stokes equations. Calcolo 1984;21(4):337–44.
[26] Osher S. Riemann solvers, the entropy condition, and difference approximations. SIAM J Numer Anal 1984;21(2):217–35.
[27] Noh WF, Woodward P. SLIC (simple line interface calculation). Proc Fifth Int Conf Numer Methods Fluid Dyn 1976;59:330–40.
[28] Shashkov M, Wendroff B. The repair paradigm and application to conservation laws. J Comput Phys 2004;198(1):265–77.
[29] Nguyen KD, Guillou S, Chauchat J, Barbry N. A two-phase numerical model for suspended-sediment transport in estuaries. Adv Water Resour 2009;32:1187–96.
[30] Badr S, Gauthier G, Gondret P. Erosion threshold of a liquid immersed granular bed by an impinging plane liquid jet. Phys Fluids 2014;26:023302.
[31] Nguyen D, Zapata MU, Gauthier G, Gondret P, Bang DPV. A two phase numerical model for the water injection dredging (WID) technology: an unified formulation for continuum mechanic. In: 11th international conference on hydroinformatics, CUNY Academic works; 2014. p. 1–6.
[32] Chauvin GE, Cesare GD, Schwindt S. Modelling of plunge pool scour evolution in non-cohesive sediments. Eng Appl Comput Fluid Mech 2014;8(4):477–87.
[33] Pagliara S, Hager WH, Minor H-E. Hydraulics of plane plunge pool scour. J Hydr Eng 2006;132(5):450–61.
[34] Pagliara S, Hager WH, Unger J. Temporal evolution of plunge pool scour. J Hydr Eng 2008;134:1630–8.
[35] Gladstone C, Phillips JC, Sparks RSJ. Experiments on bidisperse, constant-volume gravity currents: propagation and sediment deposition. Sedimentology 1998;45(5):833–43.
[36] Manenti S, Sibilla S, Gallati M, Agate G, Guiandalini R. SPH simulation of sediment flushing induced by a rapid water flow. J Hydraul Eng 2012;138:272–84.
[37] Boillat J-L, Cesare GD, Schleiss A, Oehy C. Successful sediment flushing conditions in alpine reservoirs. In: Proceedings international workshop and symposium on reservoir sedimentation management; 2000. p. 47–59.

Please cite this article as: S. Boyaval et al., A semi-Lagrangian splitting method for the numerical simulation of sediment transport with free surface flows, Computers and Fluids (2018), https://doi.org/10.1016/j.compfluid.2018.04.002